

Response of Thermohaline Circulation to Changes in Precipitation

Yuki Yasuda

October 1, 2013

1 Introduction

The oceanic thermohaline circulation has important roles in the global heat transport and hydrological cycle by transporting heat from low latitudes to high latitudes and by transporting freshwater from high latitude to low latitude. Especially, the marginal sea (e.g., Labrador and Greenland Seas) is important for the thermohaline circulation, because it is one of a few origins of the deep ocean water [4] and because waters such as Labrador Sea water spread widely [9]. However, its dynamics is not very clear.

One method for analyzing a complicated system is to use the reduced system in which the degree of freedom is lower than in the original system. [8] proposed the idealized two-dimensional dynamical system (DS) for the thermohaline circulation, i.e., two-box model. In this model, the exchange between the boxes is due to the mean flow directly driven by the pressure gradient. However, large-scale flow in the ocean is approximately geostrophically balanced, and hence, the assumption used for the two-box model is not valid.

[5, 7] derived the new two-dimensional DS. He considered the idealized marginal sea (Fig. 1). The boundary current is geostrophically balanced, which flows along the topographic contours because of the potential vorticity conservation and the pressure gradient between the boundary current and the interior region. On the other hand, in the interior region, the sea water is cooled by the atmosphere and becomes fresh by the precipitation. Thus, it is considered that baroclinic instability occurs due to the density difference between the boundary current (warm and salty) and the interior region (cold and fresh). The heat and salt transports are driven by these baroclinic eddies.

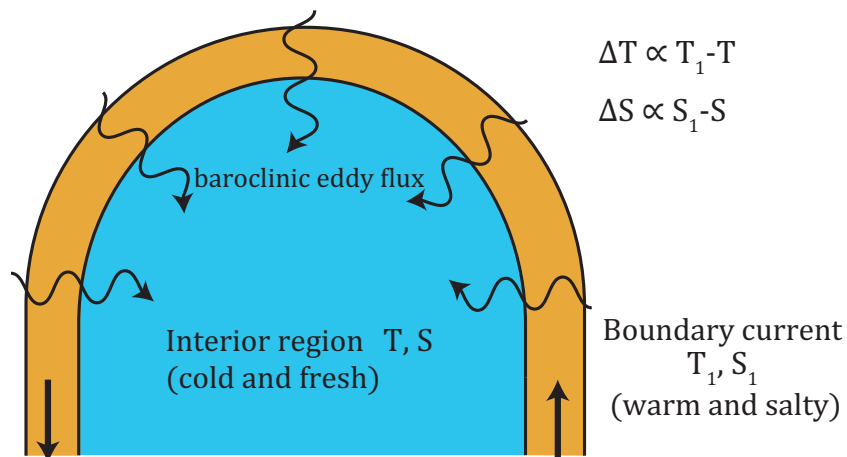


Figure 1: Schematic picture of the idealized marginal sea.

It is easy to understand the physics in the reduced DS, however, it is not clear whether this DS describes the correct physics inherent in the original system. [5, 7] compared the steady-state solutions obtained by the DS with those obtained by the numerical model in which mesoscale eddies are explicitly resolved. He showed that the derived DS well predicts the behaviors of the numerical model for the steady states.

In this study, we extend the DS proposed by [7] to the case with time-dependent precipitation and examine its behavior. After that, in order to confirm the validity of the DS, results by the DS are compared with those by the numerical model.

The structure of this report is as follows. In Section 2, we extend the DS and review its properties under the steady precipitation. In Section 3, the DS with periodic precipitation is examined. It is shown that there are three kinds of limit cycle. In Section 4, the results obtained by the DS in Section 3 are compared with results of the numerical model. It is shown that the DS qualitatively well describes the behaviors of the numerical model. In Section 5, the DS with step function precipitation is examined, and especially, transition time between the fixed points is analyzed. In Section 6, it is shown that the DS qualitatively well describes the behaviors of the numerical model also in the case of the step function precipitation. In Section 7, causes for the quantitative disagreement between the DS and

the numerical model are discussed. In Section 8, summary is made.

2 Two-dimensional non-autonomous dynamical system

2.1 Governing equations

The most important quantities for the idealized marginal sea (Fig. 1) are temperature and salinity, because the other quantities (e.g., baroclinic velocity and strength of the meridional overturning circulation) can be deduced from them. Thus, we consider the following fundamental equations for temperature and salinity:

$$\frac{\partial \bar{T}}{\partial t} + \nabla \cdot (\bar{\mathbf{u}}\bar{T}) = -\nabla \cdot (\overline{\mathbf{u}'T'}) + Q_T, \quad (1)$$

$$\frac{\partial \bar{S}}{\partial t} + \nabla \cdot (\bar{\mathbf{u}}\bar{S}) = -\nabla \cdot (\overline{\mathbf{u}'S'}) + Q_S, \quad (2)$$

where a bar represents the time average, and Q_T and Q_S represent non-conservative forcings (e.g, atmospheric cooling and precipitation). In the marginal sea, the time scale of baroclinic eddy is determined mainly by the relaxation time of the atmospheric cooling, because eddies are considered to run away from the baroclinic region. In this case, it is enough to take three-month average.

Four assumptions are made following [7] for deriving the reduced DS:

1. Temperature T_1 and salinity S_1 of the boundary current are constant.
2. Interior region is well-mixed, and temperature T and salinity S are constant there.
3. The magnitude of eddy flux is much larger than that of mean flux.
4. Integrated eddy fluxes are parametrized as follows:

$$\int \overline{\mathbf{u}'T'} dS = \alpha V \Delta T = \alpha \beta |\Delta T - \Delta S| \Delta T, \text{ and}$$

$$\int \overline{\mathbf{u}'S'} dS = \alpha V \Delta S = \alpha \beta |\Delta T - \Delta S| \Delta S.$$

The first assumption is made for simplicity. The second assumption is based on the fact that the interior region is well-mixed when the deep convection occurs there. The third assumption is based on the fact that the mean boundary current flows approximately along the topographic contours. The fourth assumption is made for closing the governing equations. In the above

parameterization, α and β are the constants given by the characteristic values of topography, Coriolis parameter, basic density, and thermal and haline expansion coefficients [7]. ΔT and ΔS are the differences of mean temperature and mean salinity between in the boundary current and in the interior region.

The two-dimensional non-autonomous DS is obtained from (1) and (2) as follows:

$$\frac{d\Delta T}{dt} = -\Delta T |\Delta T - \Delta S| + \frac{2\mu}{\epsilon}(1 - \Delta T), \quad (3)$$

$$\frac{d\Delta S}{dt} = -\Delta S |\Delta T - \Delta S| - \frac{\gamma_0}{4\epsilon} - \frac{\gamma'(t)}{4\epsilon}, \quad (4)$$

where each quantity is non-dimensionalized and the non-dimensional numbers (ϵ , μ and γ_0) are introduced following [7]. The first terms in the right hand sides (RHS) of (3) and (4) represent the baroclinic eddy fluxes which are down gradient. The second term in the RHS of (3) represents the atmospheric cooling, which forces ΔT to be 1. The relaxation time is determined by μ^1 . The second and the third terms in the RHS of (4) represent the constant basic and the time-dependent nets evaporation minus precipitation, respectively. Precipitation is basically dominant at high latitudes, meaning the negative γ_0 . In this study, $\epsilon = 0.15$, $\frac{\mu}{\epsilon} = 0.05$, and $\frac{\gamma_0}{\epsilon} = -0.1$ are taken unless otherwise specified. These values are considered to be close to those for Labrador Sea [7].

It should be emphasized here that the first assumption is not critical and can be removed easily by adding the tendencies of T_1 and S_1 to the RHS of (3) and (4), respectively. Especially, γ' can be considered to contain the tendency of S_1 , i.e., $\frac{dS_1}{dt}$.

The system (3) and (4) can be regard as the following three-dimensional ‘‘autonomous’’ DS:

$$\frac{d\Delta T}{dt} = -\Delta T |\Delta T - \Delta S| + \frac{2\mu}{\epsilon}(1 - \Delta T), \quad (5)$$

$$\frac{d\Delta S}{dt} = -\Delta S |\Delta T - \Delta S| - \frac{\gamma}{4\epsilon} - \frac{\gamma'(\Theta)}{4\epsilon}, \quad (6)$$

$$\frac{d\Theta}{dt} = \omega. \quad (7)$$

Note that the phase space is $\mathbb{R}^2 \times S^1$. We treat the two-dimensional non-autonomous DS unless otherwise specified.

¹ ϵ is the geometrical parameter, and hence, is not related to the thermodynamical properties of the ocean.

2.2 General properties

It can be shown that ΔT and ΔS are not divergent in time when $\gamma'(t)$ is finite. In other words, the trajectory remains in the finite region of the phase space. $\frac{d\Delta T}{dt}$ is positive at $\Delta T = 0$ and negative at $\Delta T = 1$. This means that $0 < \Delta T < 1$ when the initial value of ΔT is between 0 and 1. Note that taking the initial value between 0 and 1 is physically reasonable, and if it is taken outside this region, ΔT enters $(0, 1)$ quickly. The same argument can be made for ΔS . Note that the volume of the above finite region in the phase space depends on the maximum and the minimum of $\gamma'(t)$.

At almost all positions, the volume in the phase space is contracted, because the divergence of the velocity $(\frac{d\Delta T}{dt}, \frac{d\Delta S}{dt})$ is negative. This fact suggests that phase points asymptotically reach a set whose volume is zero. In other words, there are not repelling fixed points or repelling closed orbits. All fixed points are sinks or saddles, and all closed orbits are stable or saddle-like. Therefore, phase points are considered to be attracted to either fixed points, limit cycles, tori or strange attractors. Note that the above statements related to contraction are not mathematically exact, because the velocity $(\frac{d\Delta T}{dt}, \frac{d\Delta S}{dt})$ is not smooth on the line of $\Delta T = \Delta S$ and the divergence of the velocity can not be defined there.

2.3 Case of the steady precipitation

For preparation, we examine (3) and (4) when $\gamma'(t) = 0$. Figure 2(a) shows the vector field in the phase space. Note that all vectors are normalized at unity. The solid (dashed) curves represent the nullclines where $\frac{d\Delta T}{dt}(\frac{d\Delta S}{dt}) = 0$. It is found that there are three fixed points: stable spiral (haline mode), saddle (unstable thermal mode), and stable node (stable thermal mode).

Figure 2(b) shows the vector field in which $\frac{\gamma_0}{\epsilon} = 0.1$, i.e., evaporation is stronger than precipitation. This fact is reflected in the only one fixed point at which sea water is more salty in the interior region than in the boundary current (i.e., ΔS is negative).

Figure 3 shows the bifurcation diagrams for ΔT and ΔS against γ_0/ϵ . When γ_0 is positive, it is found that the saddle-node bifurcation occurs and the (stable) thermal mode disappears at the critical value γ^{critical} , while the haline mode always exists. Interestingly, the bifurcation also occurs at $\gamma_0 = 0$, in which the haline mode disappears. The (stable) thermal mode only exists when γ_0 is negative.

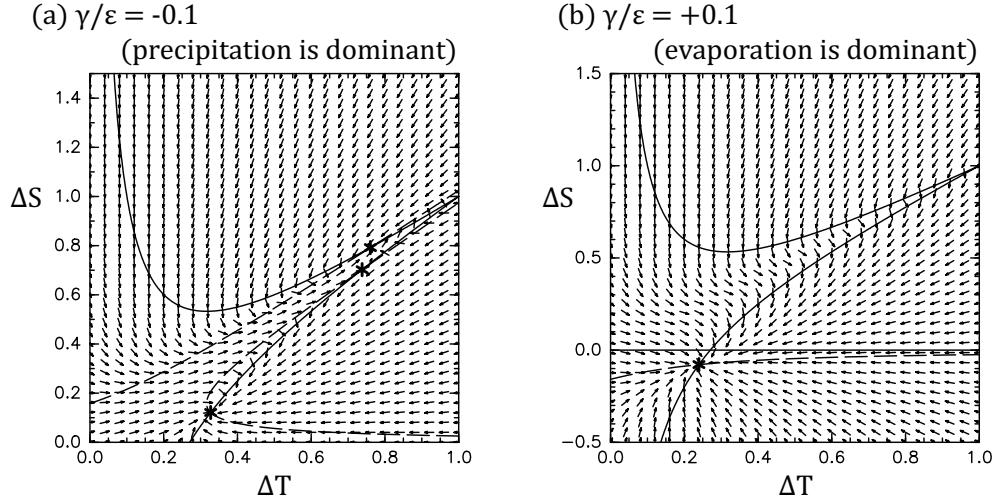


Figure 2: Vector fields, nullclines, and fixed points in the phase space. All vectors are normalized at unity. The solid (dashed) curves represent the nullclines where $\frac{d\Delta T}{dt} (\frac{d\Delta S}{dt}) = 0$.

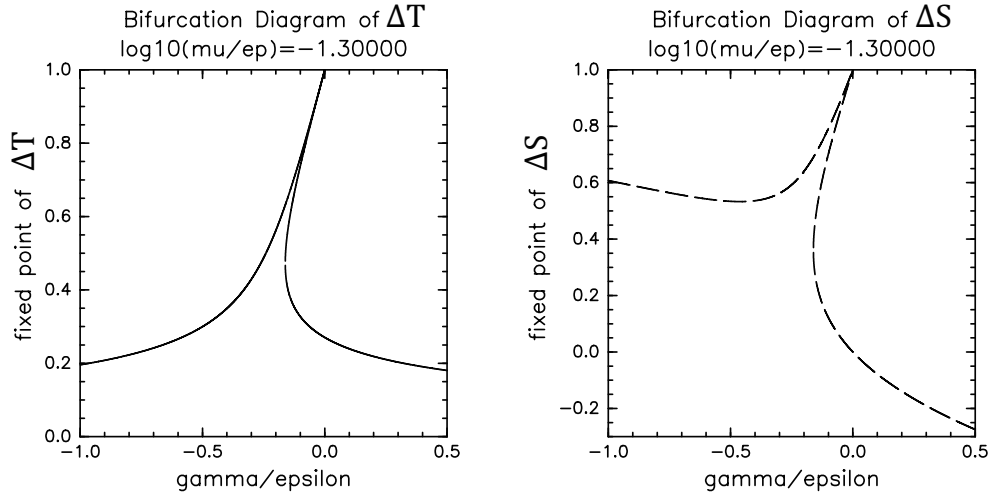


Figure 3: Bifurcation diagrams for ΔT and ΔS against γ_0/ϵ .

3 Examination of the case of periodic precipitation by the dynamical system

In this section, we examine the DS with the periodic precipitation: $\gamma'(t) = A \sin(\omega t)$ where A is the “negative” constant, ω is the positive constant. Equations (3) and (4) become

$$\frac{d\Delta T}{dt} = -\Delta T |\Delta T - \Delta S| + \frac{2\mu}{\epsilon}(1 - \Delta T), \quad (8)$$

$$\frac{d\Delta S}{dt} = -\Delta S |\Delta T - \Delta S| - \frac{1}{4\epsilon} \{\gamma_0 + A \sin(\omega t)\}. \quad (9)$$

Here the initial values are taken to be the steady solution without the periodic precipitation.

3.1 Small amplitude forcing

First, we examine the case of the small amplitude of γ' . It is expected that the (regular) perturbation method is valid. We derived the perturbation solution by assuming that the nonlinear terms are small enough.

The zeroth-order solution $(\Delta T_0, \Delta S_0)$ is the steady solution without γ' . The first-order solution $(\Delta T_1, \Delta S_1)$ consists of $\sin \omega t$ and $\cos \omega t$. The second-order solution $(\Delta T_2, \Delta S_2)$ consists of constant values, $\sin 2\omega t$, and $\cos 2\omega t$, because of nonlinear terms composed of ΔT_1 and ΔS_1 .

Figure 4(a) shows the phase differences between ΔT and γ' (solid curves), or ΔS and γ' (dashed curves). For each curve, the black (red) curve represents the result obtained by numerical calculation (perturbation solution). It is found that the phase differences are well predicted by the perturbation theory. Figure 4(b) shows the time averaged second-order quantities. It is found that each quantity is well predicted by the perturbation theory when $\omega > 10^{-1}$, while its variation is qualitatively predicted when $\omega \leq 10^{-1}$. The value of A in Fig. 4 is -0.05 , while $\gamma^{\text{critical}} - \gamma_0$ is -0.0615 . This fact means that the minimum of the total gamma is very close to the critical value. It should be emphasized here that the differences between the perturbation solution and the numerical solution can hardly be recognized when $A = -0.01$.

3.2 Arbitrary amplitude forcing

Figure 5 shows the ratios of the time-averaged values obtained by numerical calculations to the steady solutions without the periodic precipitation

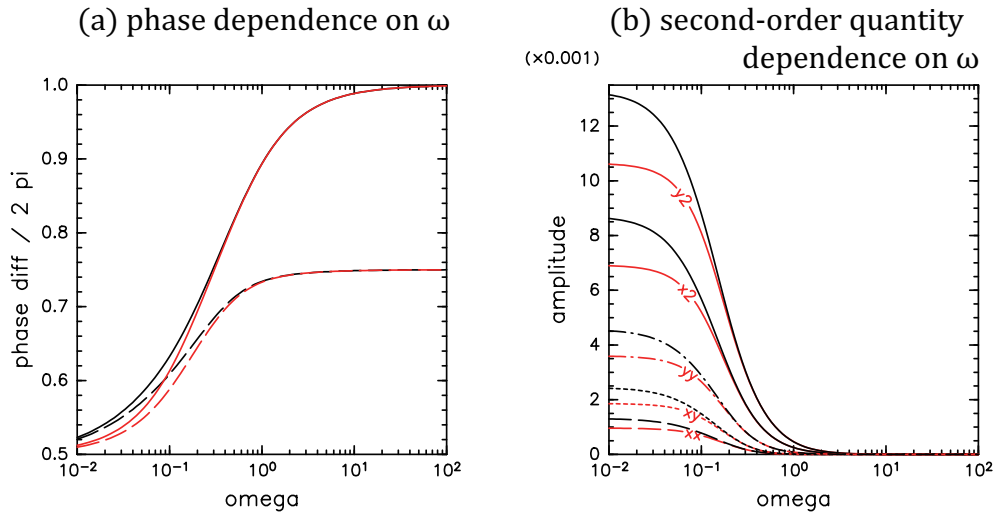


Figure 4: (a) Phase differences divided by 2π between ΔT and γ' (solid curves), or ΔS and γ' (dashed curves) plotted against ω . (b) Time averaged second-order quantities plotted against ω : $x_2 = \overline{\Delta T_2}$; $y_2 = \overline{\Delta S_2}$; $xx = \overline{\Delta T_1 \Delta T_1}$; $xy = \overline{\Delta T_1 \Delta S_1}$; and $yy = \overline{\Delta S_1 \Delta S_1}$. In both figures, the black (red) curve represents the result obtained by numerical calculation (perturbation solution).

(i.e., $\overline{\Delta T}/\Delta T_0$ and $\overline{\Delta S}/\Delta S_0$). It is found that the ratios are near unity when the amplitude of γ' (A) is small. This means that the perturbation solution is valid. Interestingly, even when A is not small enough, the ratios are near unity when ω is high enough. Actually, the perturbation solution is also valid in this case. This is because the equations (8) and (9) are approximately uncoupled when $\omega \gg \max(\Delta T_0, \Delta S_0)$ and $\frac{A}{4\epsilon} \leq \omega \cdot \max(\Delta T_0, \Delta S_0)$. This fact can be shown by the scale analysis (see Appendix A).

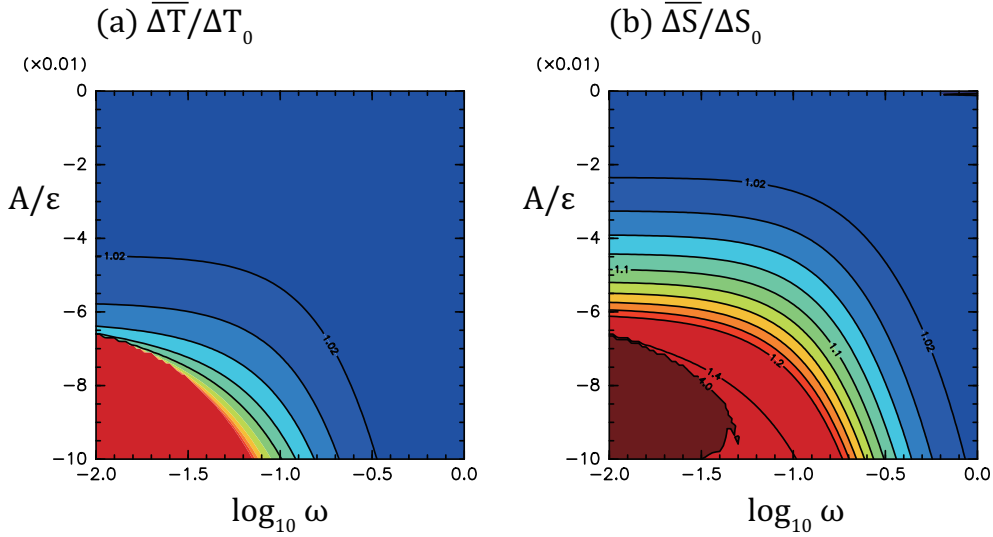


Figure 5: Ratios of the time-averaged values obtained by numerical calculations to the steady solutions without the periodic precipitation, i.e., (a) $\overline{\Delta T}/\Delta T_0$ and (b) $\overline{\Delta S}/\Delta S_0$.

In order to examine shapes of trajectories in the parameter region where ω is not high enough or the perturbation solution is not valid, the magnitude of ΔT is compared with that of ΔS . Figure 6 shows that the shapes of trajectories can be divided into three groups: ΔT (ΔS) is always greater than ΔS (ΔT) in the blue (green) region, while trajectories pass the line of $\Delta T = \Delta S$ in the red region. Note that the perturbation solution is valid in almost all blue regions by the scale analysis (see Appendix A).

The case of low ω is discussed, in which solutions can be regarded as the quasi-steady solutions. The behaviors of trajectories can be understood by

using the bifurcation diagrams (Fig. 3). In Fig. 6, the cross on the vertical axis represents $A = \gamma^{\text{critical}} - \gamma_0$. At this value, the saddle-node bifurcation occurs at the minimum of the total gamma, and hence, the state becomes the haline mode ($\Delta S > \Delta T$) even when the initial values are in the region of $\Delta T > \Delta S$. It is found that the border between the blue (thermal limit cycle) and the green (haline limit cycle) regions is very close to the cross on the vertical axis. In addition to that, the maximum of the total gamma is zero when $A/\epsilon = \gamma_0/\epsilon = -0.1$. At this value, the haline mode disappears, and the thermal mode only exists (Fig. 3). This corresponds to the border between the green and the red regions.

In the parameter region of $A/\epsilon < -0.1$, i.e., red region, the phase point passes the line of $\Delta T = \Delta S$. This is explained as follows. When the total gamma is the critical value (γ^{critical}), the saddle-node bifurcation occurs and the mode changes from the thermal mode to the haline mode. After that, the phase point moves very slowly with keeping the haline mode as the total gamma varies. However, when the total gamma is zero, the haline mode disappears and the mode changes to the thermal mode. After that, the phase point moves very slowly with keeping the thermal mode as the total gamma varies. When the total gamma is the critical value (γ^{critical}), the saddle-node bifurcation occurs again and the mode changes again from the thermal mode to the haline mode. This cycle is repeated.

So far, we have discussed the cases of low and high ω . Figure 6 shows that an interesting thing happens when ω is an intermediate value. Even when the maximum of the total gamma is negative, the trajectory can pass the line of $\Delta T = \Delta S$ around $\log_{10} \omega = -1.3$. Figure 7 shows trajectories when $A/\epsilon = -0.095$ (the maximum of the total γ/ϵ is -0.005). It is found that the trajectory is always in the region of $\Delta S > \Delta T$ ($\Delta T > \Delta S$) when ω is quite low (high), however, the trajectory passes the line of $\Delta T = \Delta S$ and looks like “8” when $\log_{10} \omega = -1.33333$. As shown in the next subsection, these three kinds of trajectories are limit cycle. Hereafter, we call the limit cycles always in the region of $\Delta T > \Delta S$ and $\Delta S > \Delta T$ thermal limit cycle (TLC) and haline limit cycle (HLC), respectively. The other limit cycle is called mixed limit cycle (MLC). The parameter region, in which each limit cycle exists, corresponds to the region in Fig. 6 as follows: TLC to blue; HLC to green; and MLC to red.

3.3 Limit cycles

In this subsection, we examine TLC, HLC, and MLC. It is confirmed that these three trajectories are limit cycles by calculating Floquet multipliers [2].

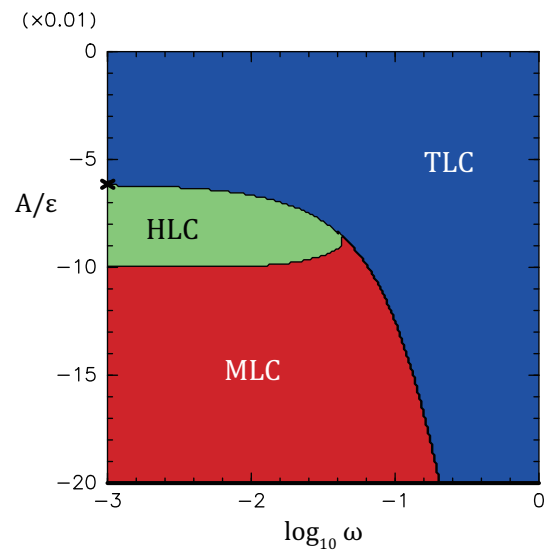


Figure 6: Parameter regions where three kinds of limit cycle exist. The cross on the vertical axis represents $A = \gamma^{\text{critical}} - \gamma_0$.

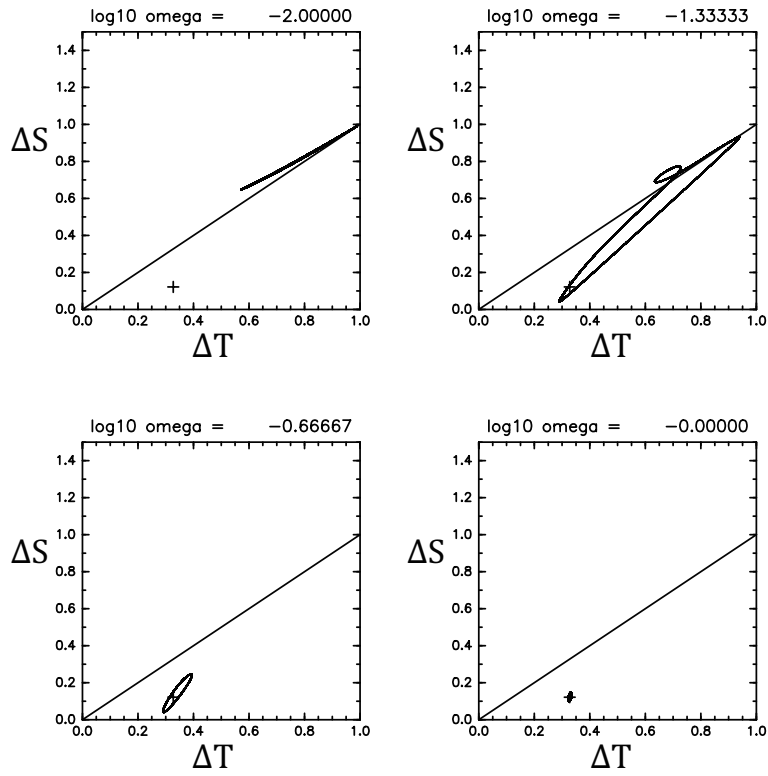


Figure 7: Trajectories when $A/\epsilon = -0.095$ (the maximum of the total γ/ϵ is -0.005). Crosses represent the initial positions.

In other words, these trajectories attract nearby points exponentially.

Figure 8 shows time cross-sections for TLC: ΔT (solid); ΔS (long dashed); $\Delta T - \Delta S$ (short dashed); and γ' (thick dashed-dotted). Note that γ' is only normalized. Figure 8(a) (ω is quite low) shows that the phase difference between ΔT (ΔS) and γ' is about 180° , while that between $\Delta T - \Delta S$ and γ' is about 0° . Figure 8(b) (ω is quite high) shows that the phase difference between ΔT and γ' is about 0° , while that between ΔS and γ' is about -90° . The sea water becomes fresh by the strong precipitation behind 90° . This leads to reduce the baroclinicity, and hence reduce the eddy flux of temperature. Thus, the sea water becomes cold by the atmospheric cooling more behind 90° . This process occurs nearly simultaneously when the precipitation period is very long (Fig. 8(a)), while it occurs in order when the period is not very long (Fig. 8(b)).

This phase relation can also be understood by using the following first-order equations for high ω :

$$\frac{d\Delta T_1}{dt} \approx \Delta T_0 \Delta S_1 = \frac{\Delta T_0}{4\omega\epsilon} A \cos \omega t, \quad (10)$$

$$\frac{d\Delta S_1}{dt} \approx -\frac{\gamma'(t)}{4\epsilon} = -\frac{1}{4\epsilon} A \sin \omega t. \quad (11)$$

Here the leading terms are only left. It is clear that the magnitudes of time-derivative terms become large as ω increases. This means that the amplitudes of ΔT_1 and ΔS_1 decrease as ω increases. This fact is reflected in decreasing the second-order quantities (Fig. 4(b)) and high accuracy of the perturbation solution when ω is high enough and A is not small enough (Figs. 5 and 6).

Figure 9 shows time cross-section for HLC: ΔT (solid); ΔS (long dashed); $\Delta T - \Delta S$ (short dashed); and γ' (thick dashed-dotted). Note that γ' is only normalized. Each parameter is the same as in Fig. 8. Figure 9(a) (ω is quite low) shows that the phase difference between ΔT (ΔS) and γ' is about 0° , while that between γ' and the “magnitude” of $\Delta T - \Delta S$ ($= |\Delta T - \Delta S|$) is about 180° . Note that $|\Delta T - \Delta S|$ is maximum when γ' is minimum. These phase relations mean that the sea water is warm and salty when precipitation is strong, because of the strong eddy flux (i.e., large baroclinicity). However, these relations are changed as ω increases.

Figure 9(b) (ω is quite high) shows that the phase difference between ΔT and γ' is about 180° , while that between ΔS and γ' is about -90° . In this case, the sea water becomes “fresh” by the strong precipitation behind 90° . This leads to increase the baroclinicity, and hence increase the eddy flux of temperature. Thus, the sea water becomes “warm” more behind 90° .

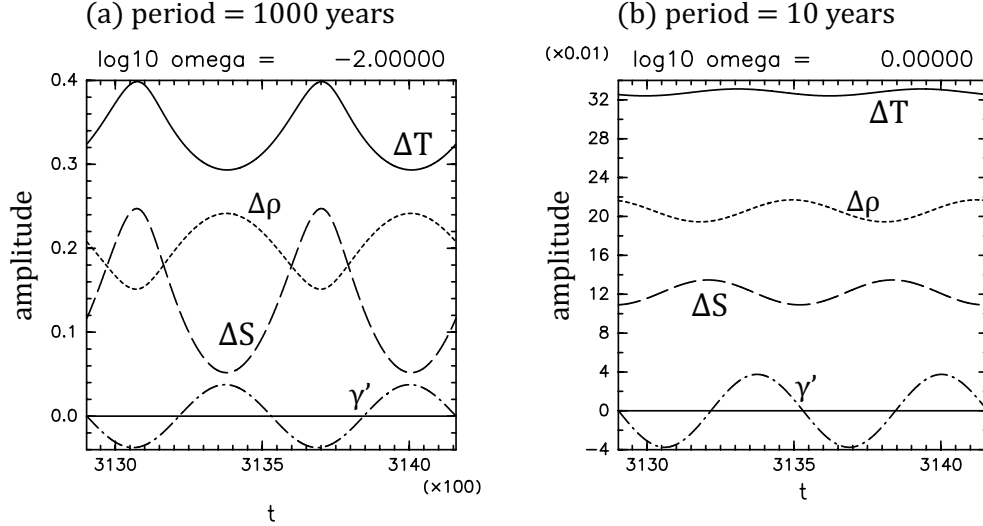


Figure 8: Time cross-sections for TLC: ΔT (solid); ΔS (long dashed); $\Delta T - \Delta S$ (short dashed); and γ' (thick dashed-dotted). γ' is only normalized.

It should be emphasized here that the effect of the fresh sea water on the baroclinicity is opposite to the case of the TLC, in which the fresh sea water reduces the baroclinicity, leading to reduce the eddy flux of temperature. The reason for the difference is that the baroclinicity (the density difference) is $\Delta T - \Delta S$ in the TLC, while that is $\Delta S - \Delta T$ in the HLC.

There is another interesting point about the phase relations between the TLC and the HLC. Examining (9) and Figs. 8 and 9, it is found that the dominant term in the eddy flux of salinity ($-\Delta S|\Delta T - \Delta S|$) is different even when its whole value is the same. For the TLC, ΔS is maximum when $|\Delta T - \Delta S|$ is minimum, while for the HLC, ΔS is minimum when $|\Delta T - \Delta S|$ is maximum. This phase-relation difference means that rotational directions of trajectories are also different: for the TLC, the direction is clockwise, while for the HLC, it is counter-clockwise.

The MLC is examined finally. Figure 10 shows the trajectory and the time cross-section of each term in (8) and (9). The atmospheric cooling and the precipitation terms are dominant when ΔT and ΔS increase, while the eddy flux terms are dominant when ΔT and ΔS decrease. This cycle is repeated only once for the TLC and the HLC, however, twice for the MLC. This is because the trajectory passes the line of $\Delta T = \Delta S$ and the eddy flux terms are proportional to $|\Delta T - \Delta S|$. When ΔT and ΔS increase

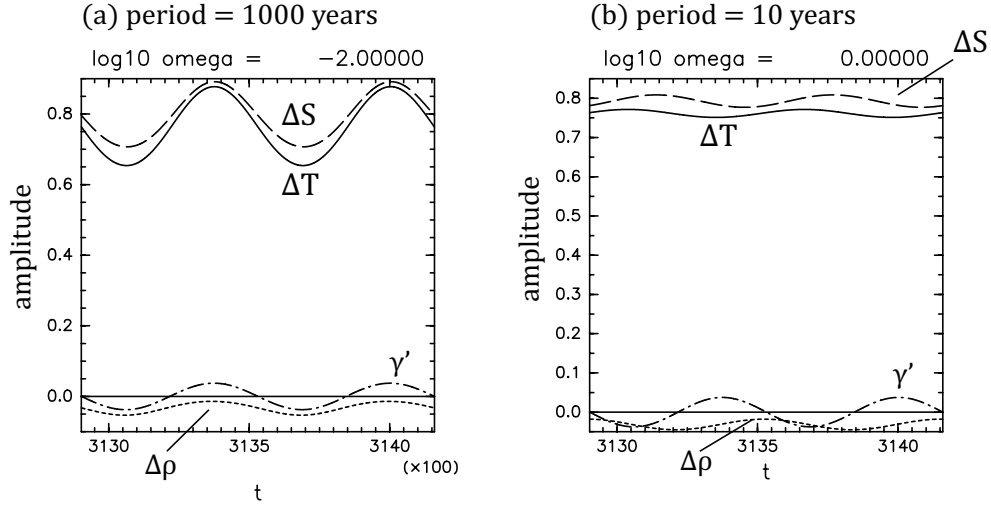


Figure 9: Time cross-sections for HLC: ΔT (solid); ΔS (long dashed); $\Delta T - \Delta S$ (short dashed); and γ' (thick dashed-dotted). γ' is only normalized.

enough after passing the line of $\Delta T = \Delta S$, the eddy flux terms reduce them. Thus, ΔT and ΔS approach the line of $\Delta T = \Delta S$ again. After that, the atmospheric cooling and the precipitation terms increase ΔT and ΔS again. If $|\Delta T - \Delta S|$ is replaced with $\Delta T - \Delta S$, ΔT and ΔS are divergent. It is considered that MLC is a limit cycle which is a mixture of the TLC and the HLC, because the rotational direction is clockwise (counter-clockwise) in the region $\Delta T > \Delta S$ ($\Delta S > \Delta T$) as the TLC (HLC).

The existence of the MLC can be discussed from a view point of an unstable limit cycle. Figures 2 and 3 show there are three fixed points for the DS without the periodic precipitation. It is considered that the thermal mode (stable node) corresponds to the TLC, while the haline mode (stable spiral) corresponds to the HLC. Thus, it is expected that an unstable limit cycle corresponding to the “unstable” thermal mode (saddle) exists. By using the single-point shooting method [2], it has been shown that the unstable limit cycle exists in some parameter regions, and that all of three limit cycles (i.e., TLC, HLC, and unstable limit cycle) expand as $|A|$ increases or ω decreases (Fig. 11). These results suggest that the unstable limit cycle helps join the TLC to the HLC as $|A|$ increases or ω decreases, because it repels nearby points. However, we have not examined the exis-

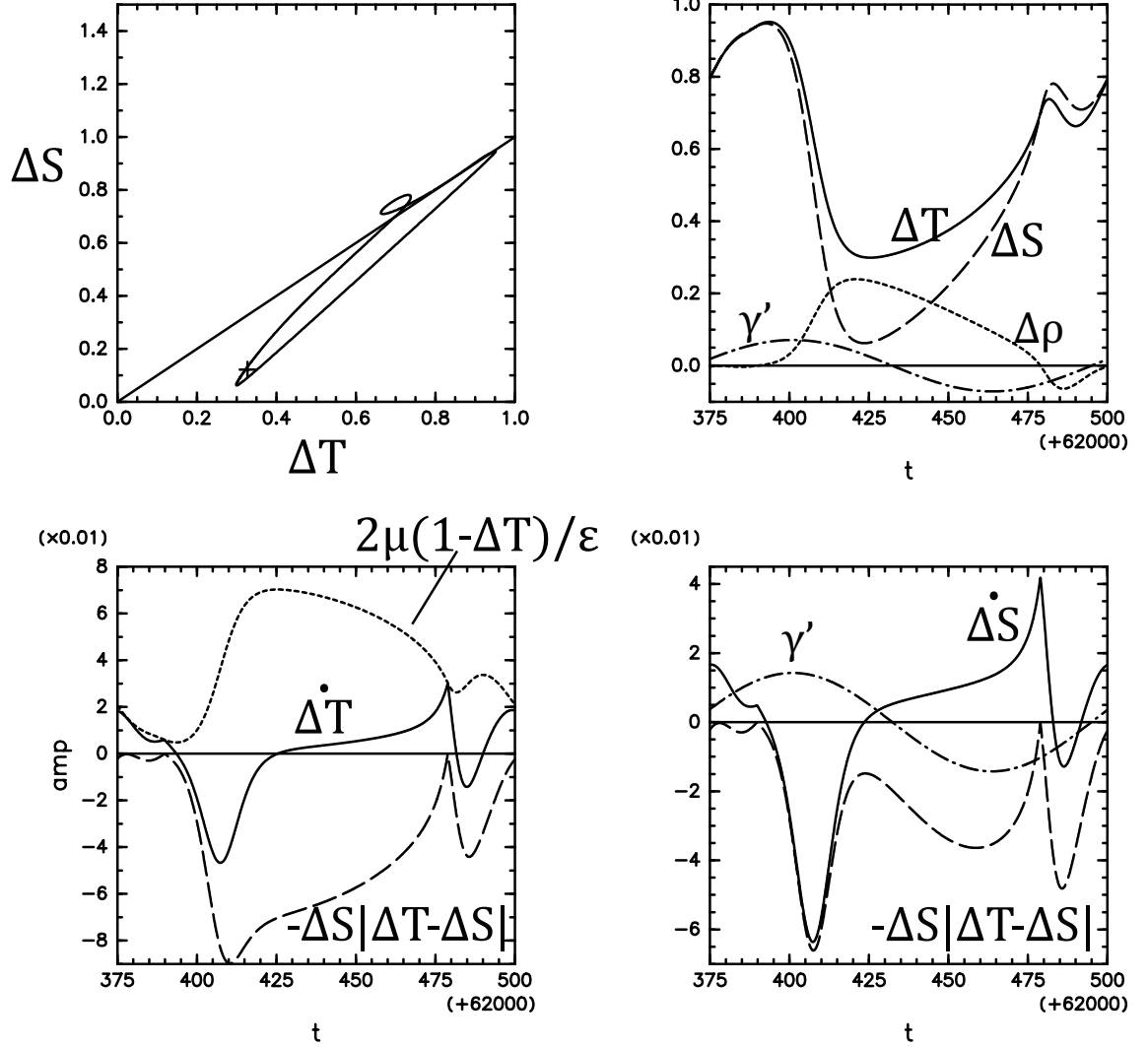


Figure 10: Top left: trajectory with the initial position (cross). Top right: ΔT (solid); ΔS (long dashed); $\Delta T - \Delta S$ (short dashed); and γ' (thick dashed-dotted). Bottom left: $\dot{\Delta T} = \frac{d\Delta T}{dt}$ (solid); $-\Delta T|\Delta T - \Delta S|$ (long dashed); and $\frac{2\mu}{\epsilon}(1 - \Delta T)$ (short dashed). Bottom right: $\dot{\Delta S} = \frac{d\Delta S}{dt}$ (solid); $-\Delta S|\Delta T - \Delta S|$ (long dashed); and γ' (thick dashed-dotted). γ' is only normalized.

tence of the unstable limit cycle in the parameter region where the MLC exists. In these parameter regions, the calculations for the unstable limit cycles are very unstable because of too large Floquet multipliers. Thus, it is necessary to use the multipoint shooting method [2] instead of the single one. In addition to that, we have to discuss the closeness of the orbits in the “three-dimensional” phase space ((5), (6), and (7)) because all of the limit cycles are trajectories in the three-dimensional phase space. The relation between the MLC and the unstable limit cycle is one of our future works.

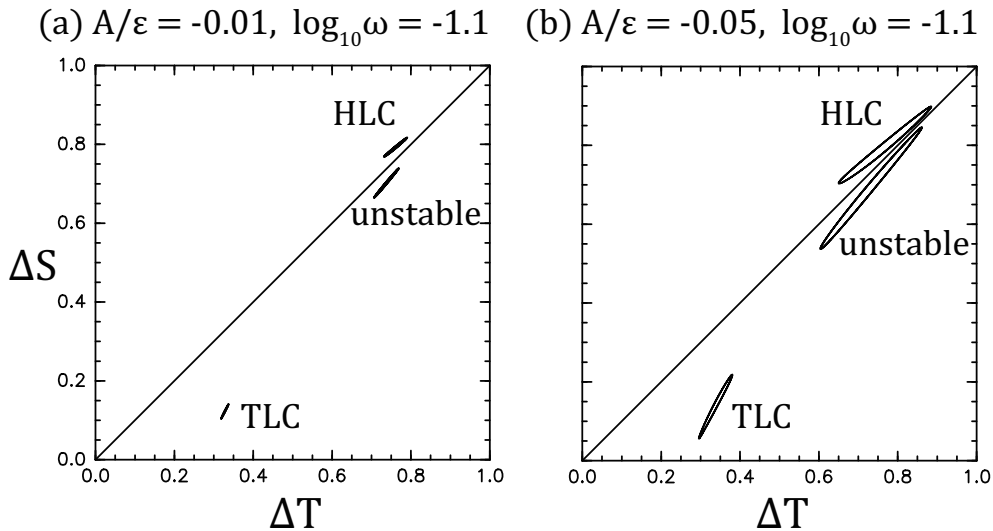


Figure 11: TLC, HLC, and unstable limit cycle in the phase space.

3.4 Dependence of limit cycles on the initial values

The dependence of TLC, HLC, and MLC on the initial values is examined. The phase constant α is introduced in the periodic precipitation: $\gamma' = A \sin(\omega t + \alpha)$. The initial values are taken to be the steady solutions of the system (8) and (9) with $t = 0$. In other words, the initial values are determined only by α . The initial values that $\Delta S > \Delta T$ are excluded in order to examine the cases where the initial states are the thermal modes.

TLC, HLC, and MLC do not depend on the initial values except for near

the boundary between the parameter regions of the HLC and the TLC (not shown), i.e., between the green and the blue regions in Fig. 6. This result means that each limit cycle has the large basin. On that boundary of the parameter space, some points are attracted to the HLC ($\Delta S > \Delta T$) even when $\Delta T > \Delta S$ initially, meaning that the basin of the HLC includes the region of $\Delta T > \Delta S$.

3.5 Chaotic behavior

At some parameters, the DS ((8) and (9)) shows chaotic behavior. Figure 12 shows two trajectories, in which the differences between their initial values are 10^{-13} for both ΔT and ΔS . Here $\frac{\mu}{\epsilon} = 0.1$, $\frac{\gamma_0}{\epsilon} = -0.2$, $\frac{A}{\epsilon} = -0.18$, $\omega = 0.2$ and $\alpha = \pi/2$ are taken. The bottom figures show the time cross-sections for the differences of ΔT and ΔS . Clearly the Lyapunov exponent is positive.

4 Examination of the case of periodic precipitation by MITgcm

In order to confirm the validity of the DS with the periodic precipitation, the oceanic circulation in the idealized marginal sea is simulated by using the numerical model. If the validity is shown, the physical understandings obtained by the DS in Section 3 can be applied to the more general oceanic circulation. The numerical model used in this study is the Massachusetts Institute of Technology General Circulation Model (MITgcm; [3]). The configuration is the same as in [6, 7] except the periodic precipitation, in which $\epsilon = 0.15$, $\frac{\mu}{\epsilon} = 0.05$, and $\frac{\gamma_0}{\epsilon} = -0.1$ as in the DS. It should be emphasized here that the MITgcm with the setting in [6, 7] explicitly resolves mesoscale eddies.

4.1 Model setting and initial value

The model domain and the forcing are shown in Fig. 13(a). The white contours show the height of the bottom topography. The region north of the sill at 1200 km latitude corresponds to the marginal sea, while the region between 1200 km and 200 km latitudes corresponds to the subpolar gyre. The other region south of 200 km latitude corresponds to the rest of the World Ocean [6], where the full depth restoring forces the state to be the uniform stratification and be the constant salinity.

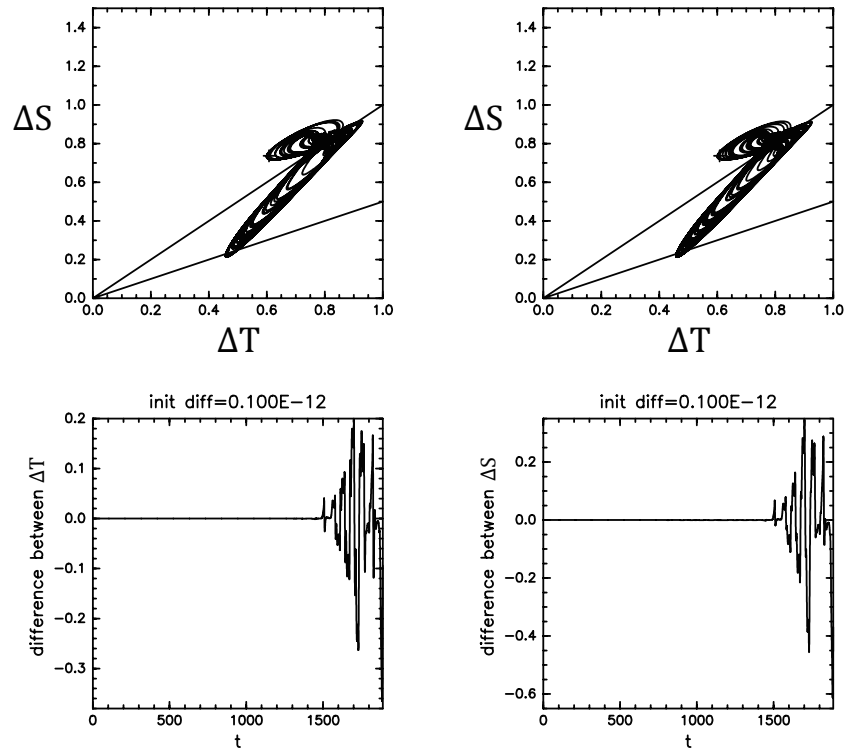


Figure 12: Top figures: two trajectories, in which the differences between their initial values are 10^{-13} for both ΔT and ΔS . Bottom figures: time cross-sections for the differences of ΔT and ΔS .

The model is run for a period of 24 years in order to obtain the initial value which can be regarded as the steady state with the steady precipitation. Figures 13(b) and 13(c) show temperature and salinity at the sea surface. The vectors in Fig. 13(c) show the horizontal velocity at the sea surface. It is found that there is a boundary current along the bottom topography, however, it is fluctuated by mesoscale eddies.

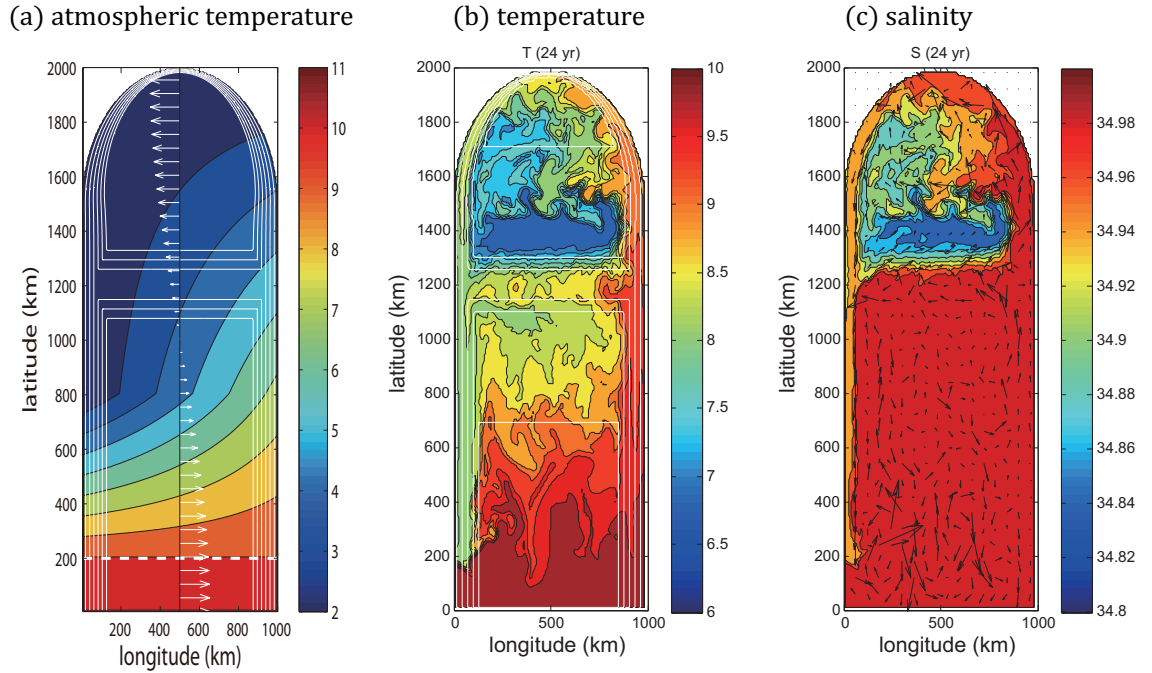


Figure 13: (a) Model domain, bottom topography (white contours; CI=300 m), wind stress (vectors), and atmospheric temperature (color). (b) Temperature at the sea surface (color). (c) Salinity (color) and horizontal velocity (vectors) at the sea surface.

After the initial spinup, the model is run with the periodic precipitation which is only in the marginal sea. The time range of integration is taken to be the doubled period of the precipitation.

4.2 Time evolutions of ΔT and ΔS

Figures 14(a) and 14(b) show the time cross-sections of ΔT , ΔS , and γ' where the periods of the precipitation are 10 and 80 years, respectively.

Here $A/\epsilon = \gamma_0/\epsilon = -0.1$ is taken for both cases. In each figure, dashed curve is obtained by the DS, while solid curve is obtained by the MITgcm. Red curves show the components having frequencies lower than or equal to the frequencies of the precipitation. It has been confirmed that these low frequency components are dominant by calculating the spectrum densities of ΔT and ΔS (not shown).

It is found that the phase relations of the DS results between ΔT , ΔS , and γ' qualitatively well correspond to those of the MITgcm results, while the amplitudes of ΔT and ΔS are much larger in the DS than in the MITgcm. These results suggest that the DS qualitatively describes the behaviors of the MITgcm, while it does not quantitatively.

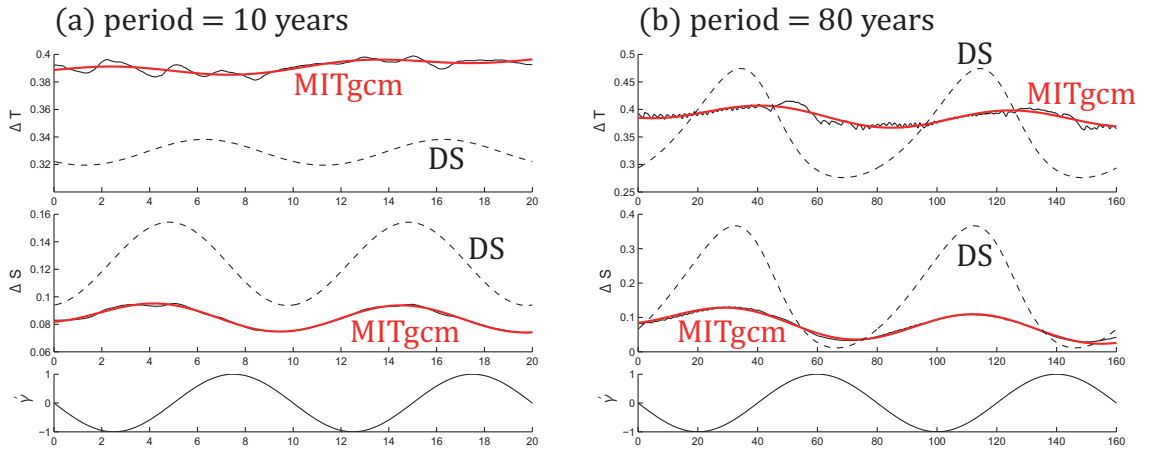


Figure 14: Time cross-sections of ΔT , ΔS , and γ' where the periods of the precipitation are (a) 10 years and (b) 80 years. In both cases, $A/\epsilon = \gamma_0/\epsilon = -0.1$ is taken. See text for details.

4.3 Quantitative evaluation of the dynamical system

In order to show the qualitative agreement between the behaviors of the DS and the MITgcm, correlation coefficients between their results are calculated. Figure 15 shows the scatter plots for the phases and the amplitudes of ΔT and ΔS . In each figure, the lateral axis shows a quantity obtained by the DS, while the vertical axis shows that obtained by the MITgcm. Here the phase at the initial time is defined as 0 rad. It is suggested that the DS qualitatively well describes the behaviors of the MITgcm.

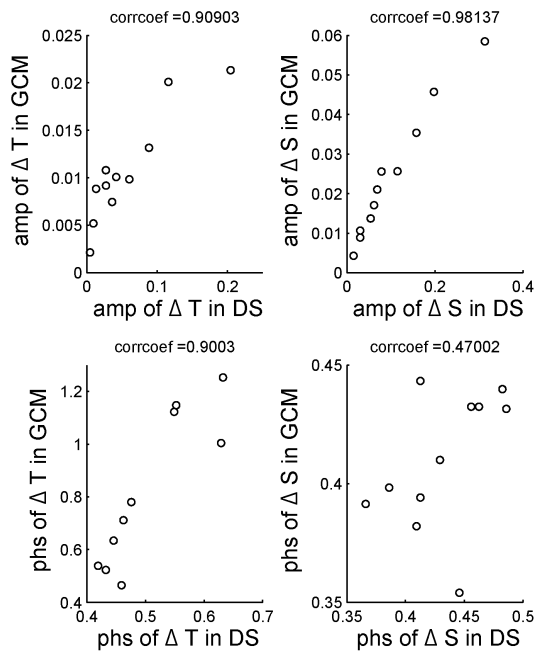


Figure 15: Scatter plots and correlation coefficients for the phases and the amplitudes of ΔT and ΔS .

One of causes for the quantitative disagreement is the difference of the transition time between in the DS and in the MITgcm. If the transition time is much longer in the MITgcm, it may take more time to increase (decrease) the amplitudes of ΔT and ΔS when the precipitation becomes strong (weak). Thus, we examine the DS with the step function precipitation in Section 5, and compare the result with that obtained by MITgcm in Section 6.

5 Examination of the case of step function forcing by the dynamical system

In this section, we examine the DS with the step function precipitation:

$$\gamma'(t) = \begin{cases} \Delta\gamma & (t \geq 0), \\ 0 & (t < 0). \end{cases} \quad (12)$$

The initial values are taken to be the steady solution without the step function precipitation. Transitions between thermal modes are only examined.

5.1 Trajectory

The fixed point instantly changes to the new one as the precipitation changes. Figure 16(a) shows the trajectories in the phase space where the cross (triangle) is the old (new) thermal mode. Figure 16(b) shows the correspondent time cross-section: ΔT (solid) and ΔS (dashed). It is found that the sea water becomes fresh and cold because the precipitation becomes strong. On the other hand, when the precipitation becomes instantly weak, the sea water becomes salty and warm (not shown).

5.2 Transition time

Transition times for ΔT and ΔS are defined as the minimum values t such that $\frac{|\Delta T(\infty) - \Delta T(t)|}{|\Delta T(\infty) - \Delta T(0)|} < 10^{-1}$ and $\frac{|\Delta S(\infty) - \Delta S(t)|}{|\Delta S(\infty) - \Delta S(0)|} < 10^{-1}$, respectively, where $(\Delta T(0), \Delta S(0))$ represents the old fixed point and $(\Delta T(\infty), \Delta S(\infty))$ represents the new one. The transition time is obtained as the average between those for ΔT and ΔS .

Figure 17 shows the transition time plotted against $\frac{\Delta\gamma}{\epsilon}$. The black curve is obtained by the numerical calculations, while the red curve is obtained by the asymptotic solutions described below. It is found that the transition

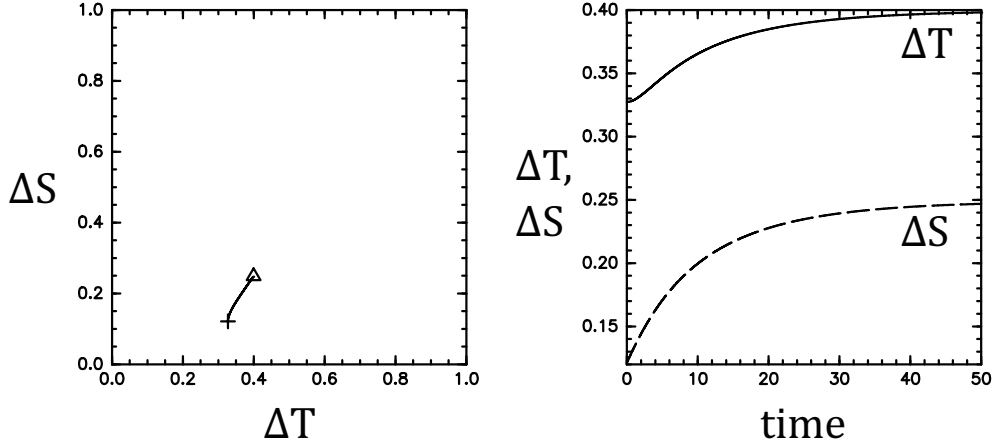


Figure 16: (a) Trajectory. The cross (triangle) is the old (new) thermal mode. (b) time cross-sections of ΔT (solid) and ΔS (dashed).

time is asymmetrical about $\frac{\Delta\gamma}{\epsilon}$. It takes more time to transition when the precipitation becomes instantly strong ($\Delta\gamma < 0$).

In order to understand the above asymmetry, the asymptotic solution is obtained by using the renormalization group method [1]. The renormalization group method is one of singular perturbation methods, which has the following features. (i) Many singular perturbation methods for ordinary differential equations (e.g., boundary layer method, WKB method, and multiple scale method) can be regarded as the renormalization group method. (ii) Particular preparations, such as the proper introduction of multiple time-scale in the multiple scale method, are not necessary. (iii) The solution is sometimes more accurate than those obtained by using other methods such as the boundary layer method.

The dependent variables are expanded as $\Delta T = \Delta T_0 + \sigma \Delta T_1 + \sigma^2 \Delta T_2$ and $\Delta S = \Delta S_0 + \sigma \Delta S_1 + \sigma^2 \Delta S_2$ where σ is considered as the small parameter and $\frac{\Delta\gamma}{4\epsilon}$ is also considered to be $O(\sigma)$. After obtaining the first-order solution, σ is taken to be unity. It is found from Fig. 17 that the transition time by the asymptotic solution well corresponds to that by the numerical solution when $|\Delta\gamma/\epsilon|$ is small, while the asymptotic solution well represents the asymmetry of the transition time about $\Delta\gamma$ in the wide range of $\frac{\Delta\gamma}{\epsilon}$.

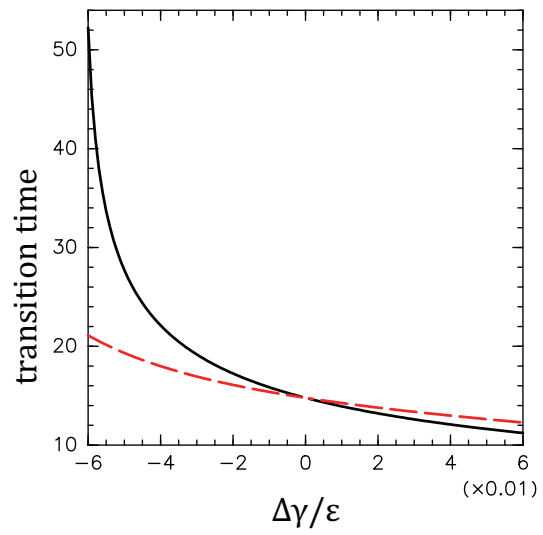


Figure 17: Transition time plotted against $\frac{\Delta\gamma}{\varepsilon}$. The black curve is obtained by the numerical calculations, while the red curve is obtained by the asymptotic solutions.

It can be found from the case of the small $|\frac{\Delta\gamma}{\epsilon}|$ that the asymmetry of the transition time in the asymptotic solution is due to the asymmetry of the eigenvalues for the new thermal mode. In fact, the magnitudes of the eigenvalues for the stable thermal mode monotonically increase as gamma increases, i.e., the precipitation becomes weak. This means that the new thermal mode starts attracting nearby points more strongly as $\frac{\Delta\gamma}{\epsilon}$ increases.

From the above discussion, the asymmetry of the transition time in the numerical solution of Fig. 17 can be explained as follows. When $\frac{\Delta\gamma}{\epsilon}$ is positive (negative), the baroclinicity of the new thermal mode is larger (smaller) than that of the old thermal mode because of the strong (weak) atmospheric cooling. This fact leads that the magnitudes of the eddy fluxes increase (decrease) as the state approaches the new thermal modes. Thus, it takes more time to transition in the case of the negative $\frac{\Delta\gamma}{\epsilon}$.

6 Examination of the case of step function forcing by MITgcm

In order to confirm the difference between the transition times in the DS and the MITgcm, the ocean circulation under the step function precipitation is simulated by using the MITgcm. The setting and the initial condition are the same as in the cases of the periodic precipitation (Section 4.1). In this section, the time range of integration is taken to be 40 years.

6.1 Time evolutions of ΔT and ΔS

Figure 18 shows the time cross-sections of ΔT and ΔS . Red curves are obtained by the second-degree-polynomial-curve fitting. Figures 18(a) and 18(b) show the cases of $\Delta\gamma = 0.4\gamma_0 < 0$, and $\Delta\gamma = -0.4\gamma_0 > 0$, respectively. It is found that the sea water becomes fresh and cold (warm and salty) when $\Delta\gamma$ is negative (positive). It is seen that ΔS approaches the new steady state, while ΔT is fluctuated. The transition time for the MITgcm is calculated only by using the data of ΔS . Here, $\Delta S(\infty)$ in the MITgcm is considered to be the value of ΔS at 40 years (the end of the numerical integration).

6.2 Quantitative evaluation of the dynamical system

Figure 19(a) shows the transition time against $\Delta\gamma/\epsilon$ in the DS (solid curve) and the MITgcm (dots). It is found that the dependence of the transition time on $\Delta\gamma$ in the MITgcm is well described by the DS, however,

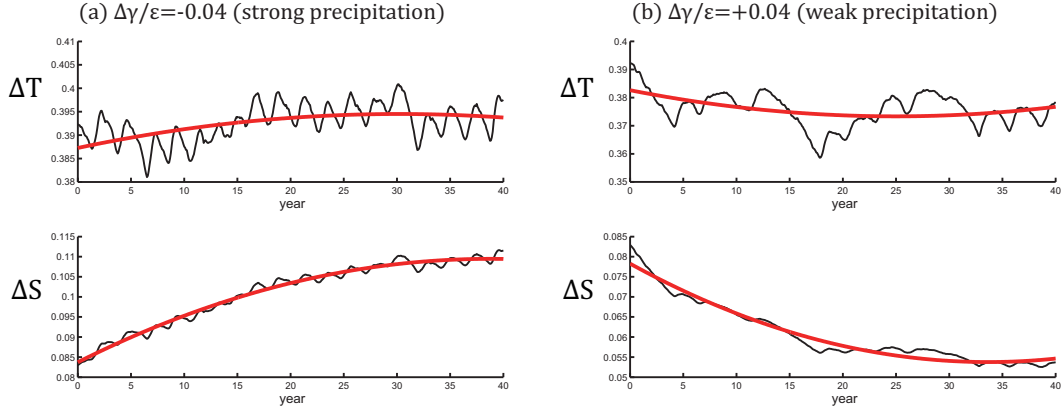


Figure 18: Time cross-sections of ΔT and ΔS in the case of step function precipitation. Red curves are obtained by the second-degree-polynomial-curve fitting.

it takes more time to transition in the MITgcm. Figures 19(b) and 19(c) show ΔT and ΔS at the end of the integration, respectively. It is clear that the DS qualitatively well describes the behaviors of the MITgcm, while it does not quantitatively.

7 Discussion

In this section, we discuss causes for the quantitative disagreement between the results of the DS and the MITgcm. In Sections 5 and 6, we have compared the transition time in the DS with that in the MITgcm. As expected before, it takes more time to transition in the MITgcm. However, this fact is not considered to be the main cause for the quantitative disagreement. In the DS with the step functional case, ΔT and ΔS change to the new equilibrium values within the “same” time-scales. Figure 19(c) shows that ΔS in the DS is very close to that in the MITgcm when $\frac{\Delta\gamma}{\epsilon} = 0.04$. Note that the transition time is shorter when $\Delta\gamma > 0$. Thus, ΔT in the DS should be also very close to that in the MITgcm, even if the transition time in the MITgcm is longer than that in the DS. However, ΔT in the DS is much smaller than that in the MITgcm when $\frac{\Delta\gamma}{\epsilon} = 0.04$. The transition time for ΔT might be longer than that for ΔS in the MITgcm, differently from in the DS.

At least, there are three possible causes for the quantitative disagree-

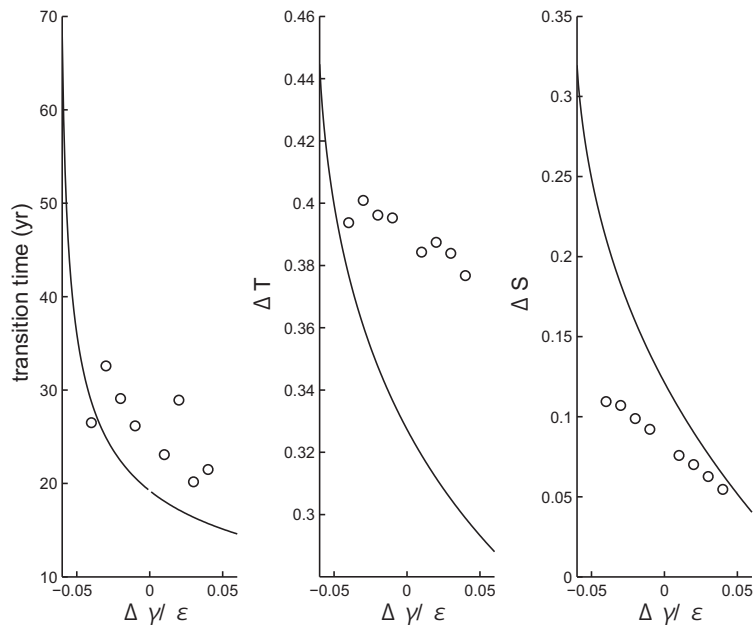


Figure 19: (a) Transition time against $\Delta\gamma/\epsilon$, (b) ΔT and (c) ΔS at the end of the integration in the DS (solid curve) and the MITgcm (dots).

ment:

1. Sensitivity of the DS to the parameters, i.e., $\epsilon, \mu, \gamma_0, A, \omega$, and $\Delta\gamma$.
The determination of the parameters have a lot of uncertainty. Thus, it may be possible to get better quantitative agreement by choosing other parameter values within the reasonable ranges.
2. Parametric resonance for the baroclinic flow.
The parameterization in the fourth assumption of Section 2 is based on the Eady problem. However, the parametric resonance may occur when the basic baroclinic flow is time-periodic. Thus, the parameterization used for the DS might not be valid.
3. Effect of changes in the spatial structure.
In the DS, changes in the spatial structures of the boundary current and the eddy are ignored, resulting from the reduction of the original system. It is possible that changes in the spatial structures affect ΔT and ΔS obtained by the spatial integration.

One of the most important future works is to compare the eddy and the mean fluxes in the DS with those in the MITgcm. Note that the mean fluxes are taken to be zero in the DS by the third assumption of Section 2. Only the eddy and the mean flux are originated in the nonlinear effects, while the atmospheric cooling and the precipitation can be regarded as the external forcings. It is expected that we can estimate the main cause for the quantitative disagreement by this comparison.

8 Summary

We extended the two-dimensional dynamical system (DS) for the idealized marginal sea proposed by [7] to the case with time-dependent precipitation.

In the case of the periodic precipitation, the DS had three kinds of limit cycle: thermal limit cycle (TLC), haline limit cycle (HLC), and mixed limit cycle (MLC). The physics of the TLC and the HLC could be understood by the regular perturbation solution. It was weakly suggested that the existence of the MLC was related to the unstable limit cycle correspondent to the saddle in the DS with the steady precipitation.

In the case of the step function precipitation, the transition time is asymmetrical about the gap of the precipitation. It takes more time to transition

when the precipitation becomes strong instantly. This asymmetry can be explained by the asymmetry of the baroclinicity in the new equilibrium state.

By comparing with results by the numerical model simulations following [7], it was shown that the DS qualitatively well described the behaviors of the numerical model, while it did not quantitatively.

Acknowledgments

I am deeply grateful to Michael Spall for proposing this project, having a lot of discussion with me, and guiding me through the summer. He also let me use his computers and kindly helped me to run the MITgcm. I am deeply grateful to Predrag Cvitanović for telling me how to analyze the periodic orbit and having a lot of discussion with me. I am grateful to Edward Spiegel for introducing me to Predrag and telling me a lot of interesting things about an application of dynamical system. I am grateful to Joseph Pedlosky and Pascale Garaud for giving helpful comments. I am grateful to Oliver Bühler for answering my questions about wave-mean flow interaction. I am deeply grateful to the coordinators of this GFD program, Claudia Cenedese, Eric Chassignet, and Stefan Llewellyn Smith for giving helpful supports. I am also grateful to Woods Hole Oceanographic Institution. I am grateful to Paul Linden for giving the principal lecture about the gravity current. I am grateful to all staff for having many interesting lectures. Finally, I would like to thank all the fellows for the great time we had in Walsh Cottage, housings, softball field, beautiful beaches, and many good restaurants and bars in Woods Hole and Falmouth. I enjoyed summer very much and learned many things.

A Scale analysis of the DS with the periodic precipitation

We separated ΔT and ΔS as $\Delta T_S + \Delta T'$ and $\Delta S_S + \Delta S'$, respectively, where $(\Delta T_S, \Delta S_S)$ is the steady solution without the periodic precipitation. Here we consider that $\Delta T > \Delta S$. The same scale analysis can be made for $\Delta S > \Delta T$. The DS ((8) and (9)) is transformed as follows:

$$\frac{d\Delta T'}{dt} = m\Delta T' + n\Delta T' - \Delta T'^2 + \Delta T'\Delta S', \quad (13)$$

$$\frac{d\Delta S'}{dt} = k\Delta T' + l\Delta T' + \Delta S'^2 - \Delta T'\Delta S' + f \sin \omega t. \quad (14)$$

Here m, n, k, l and f are the following constant numbers: $m = -2\Delta T_S + \Delta S_S - \frac{2\mu}{\epsilon}$; $n = \Delta T_S$; $k = -\Delta S_S$; $l = 2\Delta S_S - \Delta T_S$; and $f = \frac{A}{4\epsilon}$. We rescale time as $\tau = \omega t$, and coefficients (m, n, k, l) as $(m, n, k, l) = c(M, N, K, L)$ where $M, N, K, L = O(1)$. In addition to that, we introduce the new dependent variables as $x \equiv c\Delta T'/f$ and $y \equiv c\Delta S'/f$. Finally, we introduce two non-dimensional numbers $\Omega = \omega/c$ and $F = f/c^2$. Thus, equations (13) and (14) become

$$\Omega \frac{dx}{d\tau} = Mx + Ny - Fx^2 + Fxy, \quad (15)$$

$$\Omega \frac{dy}{d\tau} = Kx + Ly + Fy^2 - Fxy + \sin \tau. \quad (16)$$

There are nine cases for Ω and F . In some cases, the leading equations are linear as follows.

Table 1: The linearity/non-linearity of the leading equation

| | $\Omega \ll 1$ | $\Omega \sim 1$ | $\Omega \gg 1$ |
|-----------------|----------------|-----------------|-------------------|
| $F \ll \Omega$ | linear | linear | linear (uncouple) |
| $F \sim \Omega$ | linear | non-linear | linear (uncouple) |
| $F \gg \Omega$ | non-linear | non-linear | non-linear |

The term ‘‘uncouple’’ means that the leading equations are (10) and (11). These uncoupled cases correspond to the case where $\omega \gg \max(\Delta T_S, \Delta S_S)$ and $\frac{A}{4\epsilon} \leq \omega \cdot \max(\Delta T_S, \Delta S_S)$, because of $O(c) = \max(\Delta T_S, \Delta S_S)$.

References

- [1] LIN-YUAN CHEN, NIGEL GOLDENFELD, AND Y. OONO, *Renormalization group and singular perturbations: Multiple scales, boundary layers, and reductive perturbation theory*, Phys. Rev. E, 54 (1996), pp. 376–394.
- [2] P. CVITANOVIĆ, R. ARTUSO, R. MAINIERI, G. TANNER, AND G. VATTAY, *Chaos: Classical and Quantum*, Niels Bohr Institute, Copenhagen, 2012.
- [3] J. MARSHALL, C. HILL, L. PERELMAN, AND A. ADCROFT, *Hydrostatic, quasi-hydrostatic, and non-hydrostatic ocean modeling*, J. Geophys. Res., 102 (1997), p. 57335752.
- [4] J. MARSHALL AND F. SCHOTT, *Open-ocean convection: Observations, theory, and models*, Rev. Geophys., 37 (1999), pp. 1–64.
- [5] MICHAEL A. SPALL, *Boundary currents and water mass transformation in marginal seas*, J. Phys. Oceanogr., 34 (2004), pp. 1197–1213.
- [6] ———, *On the role of eddies and surface forcing in the heat transport and overturning circulation in marginal sea*, J. Climate, 24 (2011), p. 48444858.
- [7] ———, *Influences of precipitation on water mass transformation and deep convection*, J. Phys. Oceanogr., 42 (2012), pp. 1684–1700.
- [8] H. STOMMEL, *Thermohaline convection with two stable regimes of flow*, Tellus, 13 (1961), p. 224230.
- [9] L. D. TALLEY AND M. S. MCCARTNEY, *Distribution and circulation of Labrador Sea water*, J. Phys. Oceanogr., 12 (1982), pp. 1189–1205.